PAPER

Check for updates

Linking zeolite structures to reactivity in the carbonylation of dimethyl ether

Dong Jae Jeong,[a] Xu Wang, [iD]†[b] Namjun Park,[a] Donggyu Lee,[a] Yongkyu Lee,[a] Jong Wook Bae, [iD]*[b] Won Bo Lee [iD]*[a] and Jong Hun Kang [iD]*[a]

Carbonylation of dimethyl ether (DME) to methyl acetate (MA) is one of the key reactions for converting syngas into valuable chemicals and renewable energy sources. The reaction is predominantly catalyzed at Brønsted acid sites (BASs) on the 8-membered ring (8-MR) of the zeolite, which stabilizes the transient compound $[Z–CH_3–CO]‡$ of the rate-determining step (RDS). Although many studies focus on local descriptors, such as the RDS activation energy and enthalpy or BAS site geometry, these models often fail to fully describe the complex interplay among BAS distribution, pore connectivity, and the three-dimensional frameworks. To develop a more globalized approach for clarifying the structure-reactivity correlation, we synthesized various 8-MR-possessing zeolites, including CHA, FER, LTA, ERI, AEI, and STI with different Si/Al ratios and evaluated their activity (normalized per acid site) in the DME carbonylation reaction. PXRD, SEM(EDS), and BET characterization confirmed the successful synthesis of each zeolite, and NH_3-TPD and pyridine-IR analyses quantified their acid properties. Density functional theory (DFT) calculations show that the activation barrier of the RDS and the stability of the most abundant surface intermediate vary depending on the zeolite topology and active site environment. In this work, it was confirmed that "pocket-like" structures connecting two 8-MRs consecutively, which make 8-MR channels, have the most influential effect on catalytic behavior. Moreover, an adsorption isovolume-based descriptor, namely D_F, which captures the 3-dimensional distribution of BAS and the accessible reaction space, is introduced based on thorough geometry analyses and correlates specifically with the transition state stabilization in the RDS. It is noteworthy that MOR and FER exhibited the highest turnover frequency, correlated with their unique BAS arrangement and favorable channel geometry for transition state stabilization, as predicted by the isovolume-based descriptor proposed in this work. Consequently, extracting 3-dimensional structural descriptors that correlate with the RDS is essential for accurate prediction of structure–reactivity relationships. This contribution provides an effective design principle for untested zeolite topologies and may guide the rational design of advanced catalysts for DME carbonylation and related shape-selective processes.

1 Introduction

Acetic acid is an essential chemical in the production of adhesives, paints, and synthetic fabrics like rayon, latex, and nylon.[1–4] Generally, it is produced through catalytic methanol carbonylation processes such as the Monsanto and Cativa processes, which rely on Rh or Ir organometallic catalysts and iodide promoters. However, these processes face critical drawbacks such as the high cost of precious metal catalysts, high-pressure operating conditions (30–60 bar), and environmental challenges related to halide treatment.[5–7]

In response to these issues, acidic zeolite catalysts are considered promising alternatives for dimethyl ether (DME) carbonylation yielding methyl acetate (MA). Not only by eliminating the need for precious metals or halides but also by allowing operation under milder conditions, zeolites improve both the economic feasibility and sustainability. Moreover, converting syngas (CO + H_2) from waste-derived sources, such as biomass gasification, plastic pyrolysis, or CO_2 recycling, into

[a] School of Chemical and Biological Engineering and the Institute of Chemical Processes, Seoul National University, Seoul 08826, Republic of Korea.
E-mail: wblee@snu.ac.kr, jonghunkang@snu.ac.kr

[b] School of Chemical Engineering, Sungkyunkwan University (SKKU), 2066 Seobu-ro, Jangan-gu, Suwon, Gyeonggi-do, 16419, Republic of Korea.
E-mail: finejw@skku.edu

† Present address: Institute of Advanced Study, Chengdu University, Chengdu 610106, China.

value-added MA, not only provides environmental benefits but also marks the beginning of its role as a platform intermediate for the synthesis of a broad range of key industrial chemicals, such as methanol, ethanol, acetic acid, methyl iodide, vinyl acetate, and ketenes, *etc.*[8–10] In particular, acetic acid can be produced from methyl acetate (MA) *via* simple hydrolysis, followed by hydrogenation to yield ethanol. This sequential conversion presents a promising example of carbon capture and utilization (CCU) technology, enabling the valorization of carbon-containing by-products generated by the existing chemical industry.[11]

Several studies indicate that this DME carbonylation reaction typically takes place at Brønsted acid sites (BASs) on the 8-membered ring (8-MR) pores of zeolites, where the transition states of adsorbed reactants are effectively stabilized.[8,12–17] Notably, mordenite (MOR) and ferrierite (FER), which both contain 8-MR pore openings in their channel systems, exhibit superior reactivity. Despite considerable research into the correlation between DME carbonylation reactivity and the 8-MR structures,[18–20] there have been a limited number of comparative studies to evaluate whether these findings hold true for other 8-MR-possessing zeolites.

More in-depth studies have focused on elucidating the intrinsic role of the 8-MR structure. These investigations use density functional theory (DFT) calculations to analyze the reaction energies associated with BASs located within 8-MR pores.[21,22] By calculating energy levels and activation energies for a sequence of elementary reactions during the DME carbonylation cycle, researchers have explained why MOR and FER show favorable reactivity. The DFT calculations commonly target two key elementary steps, based on the DME carbonylation mechanism (Fig. 1): the methylation step and the CO addition step.

The methylation step involves DME or methanol interacting with BASs within the zeolite micropores, leading to hydrogenolysis and substitution of the acid site by a methyl group (eqn (1) and (2)), where Z denotes the zeolite framework.
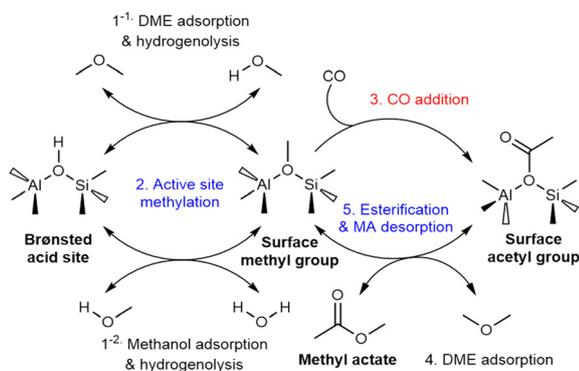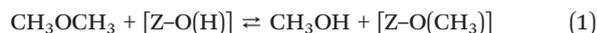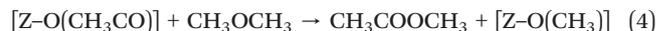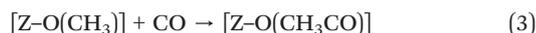
$$CH_3OCH_3 + [Z–O(H)] \rightleftarrows CH_3OH + [Z–O(CH_3)] \quad (1)$$

Fig. 1 Total catalytic cycle of DME carbonylation on the zeolite Brønsted acid site (BAS).

$$CH_3OH + [Z–O(H)] \rightleftarrows H_2O + [Z–O(CH_3)] \quad (2)$$

This step is also referred to as the "induction period" because it has been proven to be a zero-order reaction in which only the free BASs are converted to surface methyl groups (SMGs), leaving the overall reaction rate unaffected.[17]

CO addition, the key step in DME carbonylation, converts SMGs into surface acetyl groups (SAGs), which are subsequently esterified by additional DME to produce the primary product, MA (eqn (3) and (4)).

$$[Z–O(CH_3)] + CO \rightarrow [Z–O(CH_3CO)] \quad (3)$$

$$[Z–O(CH_3CO)] + CH_3OCH_3 \rightarrow CH_3COOCH_3 + [Z–O(CH_3)] \quad (4)$$

This step is widely recognized as the rate-determining step (RDS) of DME carbonylation and is generally considered as a first-order reaction. From a kinetic perspective, the methylation step is often regarded as less significant than CO addition.[13–15,17] While the extent of DME or CH_3OH concentration in the methylation step does not directly affect the rate of the MA formation under steady-state conditions, the methylation step has featured prominently in previous studies to transform BASs to SMG species that open the way to the succeeding CO addition step that has typically been supposed to be the rate-determining step (RDS).

Boronat *et al.*[14] confirmed the most active BAS for DME carbonylation in MOR by comparing DFT-predicted activation energies for the RDS and the geometric characteristics of the transient species. In this study, we adopt a similar approach but designate certain 'effective' sites (see section S1, Criteria for selecting effective Brønsted acid sites for DFT calculations in the SI), based on the crystallographic information file (cif) data from the International Zeolite Association (IZA) database (Fig. 2a).[23] Zeolites possess frameworks of repeating tetrahedral sites (T-sites) connected by bridging oxygen atoms (O-sites), each labelled as TxOy (where x = 1, 2, 3…; y = 1, 2, 3…). Also, it is well-known that several T- and O-sites within a single zeolite framework are crystallographically equivalent. Based on this nomenclature, Boronat *et al.* emphasizes that the T3O8 sites of MOR are the most reactive active sites (Fig. 2c).

The T3O8 sites are located within the 8-MR side pockets of MOR, arranged in a staggered configuration along the *c*-axis, continuously distributed along the channel (Fig. 2d). CO addition at these sites generally experiences a lower activation energy barrier than competing pathways involving other molecules such as CH_3OH, H_2O, or DME. Thus, a more favorable pathway for CO is provided when the DME carbonylation occurs at these T3O8 BAS sites. Furthermore, the orthogonal bonding of CO to the SMG ([Z–O(CH_3)] in eqn (4)) at the MOR T3O8 site facilitates the nucleophilic attack required to form acetyl species (Fig. 2c). In MOR synthesized with a low Si/Al ratio, aluminum tends to be concentrated at the T3 and T4 sites, with protons (H$^+$) favoring O8 or O10, further enhancing the catalytic reactivity of MOR.[24]
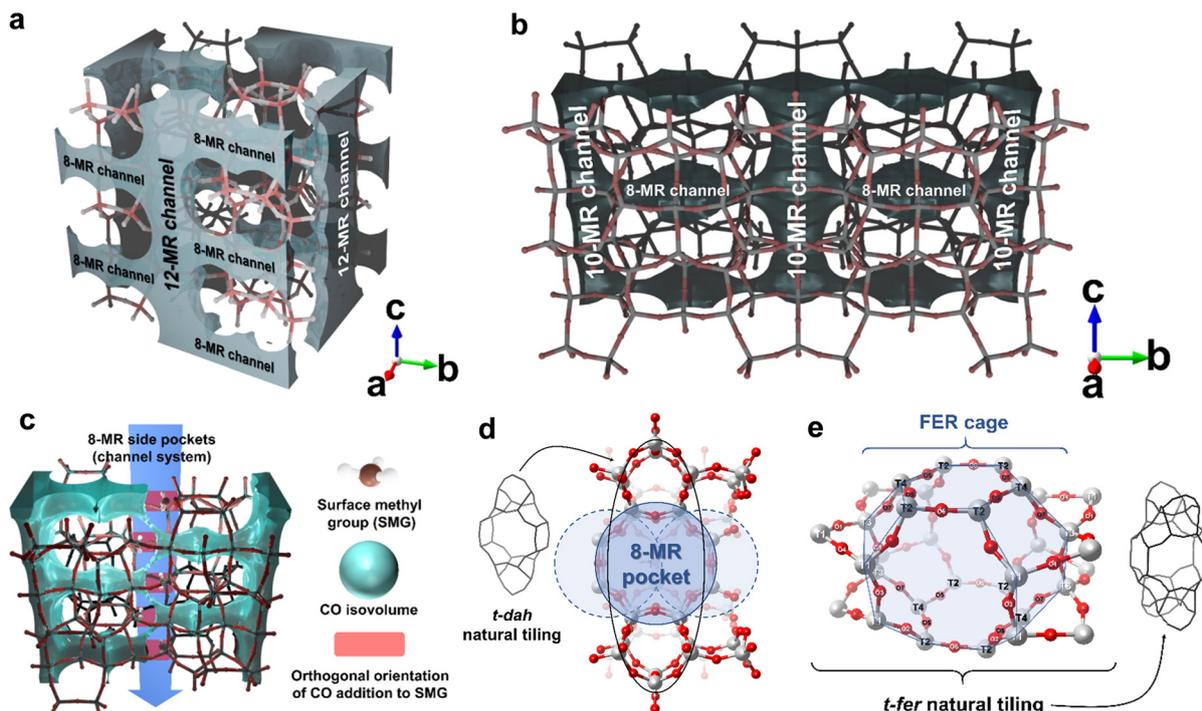
Fig. 2 MOR and FER frameworks and their substructures. (a) MOR channel system, (b) FER channel system, (c) detailed graphic of 8-MR side pockets of MOR and a series of surface methyl groups (SMGs) substituted for Brønsted acid on T3O8 sites. The reactant gases can diffuse through the cyan space, and especially in the side pocket of MOR, and can easily be added to central carbon of the SMG in the orthogonal direction (nucleophilic backside attack, see also Fig. 6); (d) schematic representation of t-dah natural tiling and staggered 8-MR pockets, which are stacked along the a-axis, and (e) schematic representation of t-fer natural tiling and the FER cage. The labels of T4O7 and T2O5 sites in FER are colored black. [Atom color] brown: carbon, white: hydrogen, gray: tetrahedral site (silicon or aluminum), red: oxygen.

Feng et al.[15] used a similar approach to analyze FER, identifying T4O7 and T2O5 (following the site numbering convention of the IZA cif files)[23] on the 6-MR unit of the 8-MR side channel as the most active sites for DME carbonylation in the FER-type zeolites (Fig. 2b and e). During the methylation step, they investigated the correlation between reaction enthalpy and the distance between the surface methyl group central carbon (C_{SMG}) and the framework oxygen (O_{FER}), noting a generally inverse relationship. However, T4O7 and T2O5 did not follow this trend, showing deviation from the lowest methylation enthalpy.

In the subsequent CO addition step, Feng et al. observed that all TxOy sites in FER require higher activation energies for CO addition compared to competing compounds, including CH_3-OH, H_2O, or DME, yet T4O7 and T2O5 show the lowest CO activation energy. Notably, the CO addition activation energy for FER (0.829–1.762 eV) determined in this study[15] is lower than that of MOR (1.451–1.866 eV).[14] In comparison, MOR has a far lower methylation enthalpy (0.008–0.363 eV)[14] than FER (0.083–0.933 eV).[15] These corroborate with Feng's conclusion that the superior reactivity of MOR is due to its lower methylation energy, suggesting a milestone for comparing the reactivity of different 8-MR zeolites.

In this study, we attempted to derive the generalized relationship between the 8-MR structure and the DME carbonylation reactivity by synthesizing not only ZSM-35 (FER)

but also SSZ-13 (CHA), zeolite A (LTA), UZM-12 (ERI), SSZ-39 (AEI), and TNU-10 (STI) within the practically feasible synthesizable range of Si/Al (note: MOR was tested using a commercial catalyst, CMOR). Details of the synthesis procedures are provided in section S2 in the SI with their representative organic structure directing agents (OSDAs) (see Fig. S3). All samples were characterized by PXRD (Fig. S4–S9), SEM(EDS) (Fig. S10), and BET analyses (Fig. S11 and Table S1) to confirm successful synthesis. NH_3-TPD and pyridine-IR (Fig. S12–S20 and Table S2) analyses were conducted for acid site quantification, and representative NH_3-TPD profiles for zeolites with the investigated topologies are provided in the cited references.[25–31] The results of characterization analyses are presented in section S3 in the SI. All samples were tested in a lab-scale tubular packed-bed reactor under the same controlled reaction atmosphere. We obtained the turnover frequency (TOF) of each sample as a normalized reactivity where the methyl acetate (MA) generation rate was divided by the density of 8-MR BASs extracted from NH_3-TPD and pyridine-IR measurements. The long-term reactivity data for the whole reaction time on stream (40 h) are presented in section S4 in the SI (Fig. S21–S26). Then we systematically correlated them with some descriptors of density functional theory (DFT), e.g., the CO addition activation energy and reaction enthalpy, side reactions with H_2O and CO (only addressed in section S6 of the SI), and geometric configuration of a transient compound [Z–CH_3–CO]‡,

all of which were adopted in many previous studies for connecting to reactivity.[14–16,32,33] However, it was confirmed that these descriptors ultimately fail to explain the DME carbonylation reactivity trends of extended 8-MR-possessing zeolites. Thus, we further considered the 3-dimensional distribution of BASs, proposing an "isovolume-based descriptor, (D_{He}, D_{CO}, and D_F)" highly correlated with the TOF evidenced from actual DME carbonylation of extended 8-MR zeolites, which can provide insightful information of the rational design of structurally diverse 8-MR zeolites.

2 Results and discussion

2.1 DME carbonylation reactivity over 8-MR zeolites

The results of the DME carbonylation reactivity test performed on the seven 8-MR zeolites selected in this study are summarized in Fig. 3. To investigate the correlation between zeolite topology and DME carbonylation reactivity, we selected Si/Al ratios ranging from 5 to 30 for each topology within the synthesis limitations available in the literature.[31,34–40] All data points represent average reactivity evaluated over a 5-hour period (30–34 h), after an initial stabilization period, which was defined as a steady state, kinetic regime with negligible
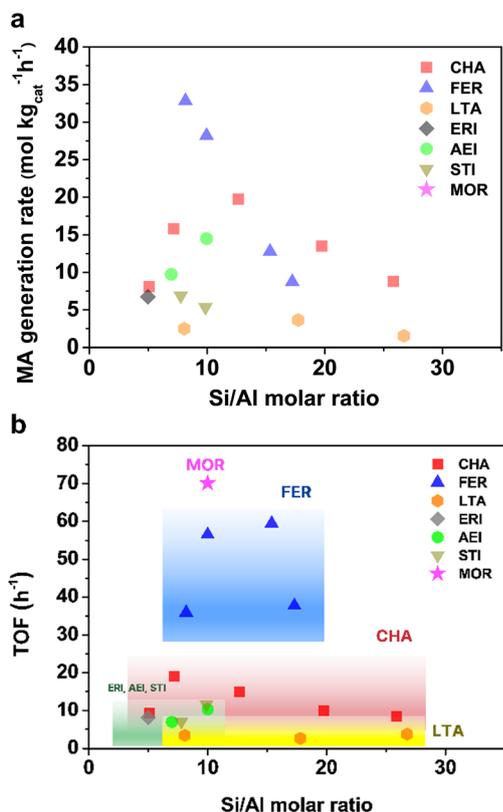

Fig. 3 Catalytic performance of each catalyst with various Si/Al ratios for DME carbonylation: (a) methyl acetate generation rate and (b) turnover frequency (TOF). All points represent actual reactivity for zeolites within the possible Si/Al range for synthesis. Reaction conditions: T = 165 °C, P = 2.0 MPa, space velocity = 2000 L (kg_{cat}^{-1} h^{-1}); feed gas composition: DME/CO/N_2 (mol%) = 4.5/90/5.5 for 40 h.

deactivation. Under mild reaction conditions, which are a strict kinetic regime (T = 165 °C, DME/CO/N_2 = 4.5/90/5.5 mol%, P = 2.0 MPa), the product selectivity of each zeolite was limited to MA and unconverted DME. Consequently, DME conversions served as the primary measure and were correlated directly with zeolite topology.

The BASs of the selected zeolites were evaluated using NH_3-TPD and pyridine IR analyses. Pyridine IR was particularly effective for FER and MOR zeolites, where the focus was placed on 8-MR acid sites while minimizing the contributions from channels wider than 10-MR. Since a pyridine molecule (~5.7 Å, in kinetic diameter) is larger than the pore size of 8-MR pore channels (~3.5 × 4.9 Å^2), pyridine selectively adsorbs on BASs within wider channels (see Fig. S1), thereby allowing to identify the influence from non-8-MR BASs at a wavenumber of 1540 cm^{-1} (see Table S2 and Fig. S18). Conclusively, the turnover frequency (TOF) for each zeolite is presented in Fig. 3b, calculated as: TOF (h^{-1}) = MA generation rate (mmol g_{cat}^{-1} h^{-1})/ 8-MR BAS density (mmol g_{cat}^{-1}). Here, the 8-MR BAS density denotes an estimated concentration of strong BASs located in 8-MR pockets, obtained from the high-temperature NH_3-TPD component, and for MOR and FER, the values after subtracting the pyridine-accessible Brønsted acid sites in 10-MR or wider channels were determined by Py-IR at 165 °C. This procedure provides an approximate but internally consistent measure of carbonylation-relevant 8-MR BASs across all frameworks. The possibility of falsified kinetics by intracrystalline diffusion was ruled out by verifying that two CHA samples, with similar Si/Al ratios but significantly different crystal sizes, exhibited comparable apparent TOF values (see Fig. S2), despite CHA having the narrowest pores [3.6 × 3.6 Å] and thus being the most diffusion-sensitive framework among the zeolites studied.

Most zeolites had maximum MA generation rate values in the range of Si/Al elemental ratios within 7–10, consistent with prior investigations on CHA[16] and FER[26] regarding DME carbonylation. This is because this range strikes a good balance between keeping enough Brønsted acidity and not overcrowding the micropores too much.[41–43] The apparent 8-MR BAS density (in particular for CHA) shows a "volcano-type" dependence on Si/Al, because at very low Si/Al, Al-site pairing and increased "NH_3-philicity" reduce the fraction of sites expressed as strong, well-isolated 8-MR Brønsted acids in the high-temperature NH_3-TPD component, whereas at very high Si/Al the total number of framework Al (and hence BAS) decreases, so the population of strong 8-MR BASs seems to be maximized at intermediate Si/Al. In addition, 7–10 is effectively the only Si/Al window in which phase-pure CHA, FER, AEI, STI, LTA, and MOR could be reproducibly synthesized with their respective OSDAs in this work, so the cross-topology TOF comparison is restricted to catalysts within this range. ERI could be obtained reproducibly only at lower Si/Al (~5) under our synthesis conditions and is therefore represented by a single composition in Fig. 3. ERI (with an Si/Al ratio of ca. 5) exhibited a TOF of 8.1 h^{-1}, whereas AEI (7.0) and STI (7.8) showed TOFs of 6.9 h^{-1} and 7.1 h^{-1}, respectively. This shows that, despite having only one data point due to the synthetic constraint, ERI will follow a TOF trend

similar to AEI and STI. According to Fig. 3b, even though all the zeolites share the same 8-MR structure, their TOFs vary depending on the topology. Within the Si/Al ratio range of 5 to 10, the reactivity order was found to be MOR > FER > CHA > ERI ≈ AEI ≈ STI > LTA.

By considering the 8-MR BAS density, the acid sites responsible for DME carbonylation were fully accounted for. However, since the catalysts still show different TOFs, it is clear that not only the acid site properties but also the intrinsic framework structures play a crucial role in determining the DME carbonylation reactivity. To gain in-depth insights into the relationship between structure and reactivity, as mentioned in the final part of section 1, this study applied two main approaches—1. DFT calculations and 2. geometric structures of a transient compound [Z–CH$_3$–CO]‡—used in previous research to explain different reactivity orders. Sections 2.2 to 2.3 contain critical results showing that these conventional methods were inadequate to explain the reactivity order of investigated zeolite samples. Section 2.4 will finally present and explain the 'key descriptor' influencing the DME carbonylation reactivity of different zeolites possessing diverse 8-MRs, demonstrating that this descriptor best accounts for the reactivity observed in the zeolites investigated in this study.

2.2 DFT analysis of the rate-determining transition state

Numerous DFT calculations have been conducted to determine the acid sites with the highest reactivity by comparing the activation energy of the RDS.[13–16,32,33] Although the details vary among these studies, they commonly evaluate both the activation energy and reaction enthalpy of the RDS at the TxOy sites of each zeolite. Overall, these findings conclude that the CO addition, which takes place primarily in and around the 8-MR pores, is the most crucial step influencing the DME carbonylation, albeit with varying levels of significance.

Guided by these results, we focused on the specific TxOy sites located in or near 8-MR (referred to here as effective

aluminum tetrahedral sites, or Al T sites) for all investigated topologies, as summarized in Table 2. Selected additional sites, essential for verification and extended discussion, are marked with a (see SI section S1). Table 2 also includes the results of the DFT calculation for both the methylation and CO addition steps across the examined TxOy sites, which are further supported by energy diagrams of each step (methylation and CO addition steps) in the SI section S5 (Fig. S27–S45). In particular, Fig. S41–S45 illustrate the whole sequential process from the initial BAS-mediated methylation step through CO addition, ultimately leading to the formation of the transient compound [Z–CH$_3$–CO]‡. To help readers clearly understand which elementary steps contribute to the energies summarized in Table 2, we even address one of these diagrams (CHA T1O4 case) in Fig. 4 as a representative.

Fig. 5 depicts the relationship between DFT-calculated energy values and the average TOF for each topology. To facilitate a quantitative comparison of DME carbonylation reactivity, we correlated the average TOF values, which were acquired from catalysts with Si/Al ratios ranging from 7–10 (the appropriate Si/Al ratio range that allows comparison between different zeolite topologies), with (a) the methylation enthalpy, (b) the CO addition activation energy, and (c) the CO addition enthalpy of the analyzed TxOy sites. Furthermore, the average values for each topology are represented by larger and lighter markers to illustrate their representative values (see Fig. 5). For the FER and LTA, the data points were calculated by considering the T sites highlighted with a in Table 2, identified as the most likely TxOy sites for these frameworks (see Fig. 6 and SI section S1). In other topologies, the effective TxOy sites were evenly distributed throughout the 8-MR pores, without a preference for any specific region; these are represented as larger and lighter markers, calculated as the average values in Table 2.

As shown Fig. 5a, FER shows the highest TOF among the zeolites investigated. However, its methylation enthalpy does not appear to be more favorable than those of other topologies. Even the methylation energy at the most effective TxOy site
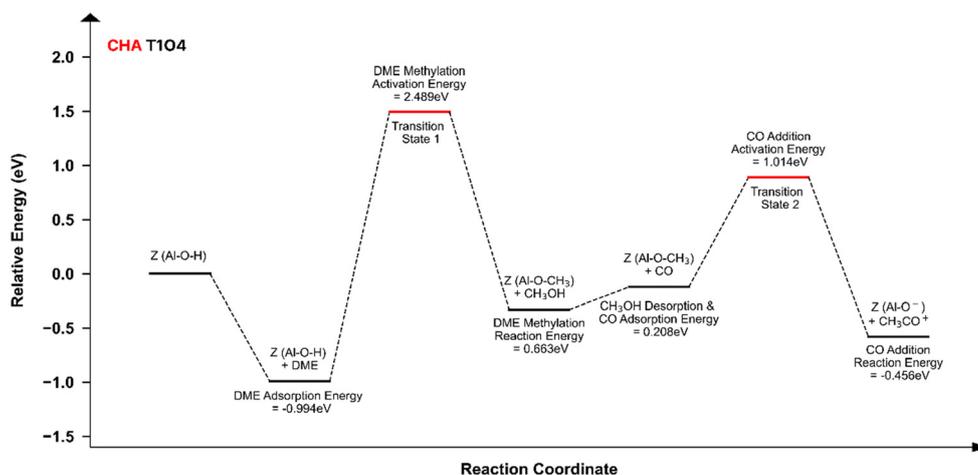

Fig. 4 Full scheme of two key steps on the DME carbonylation (methylation and CO addition step) energy diagram for CHA T1O4.
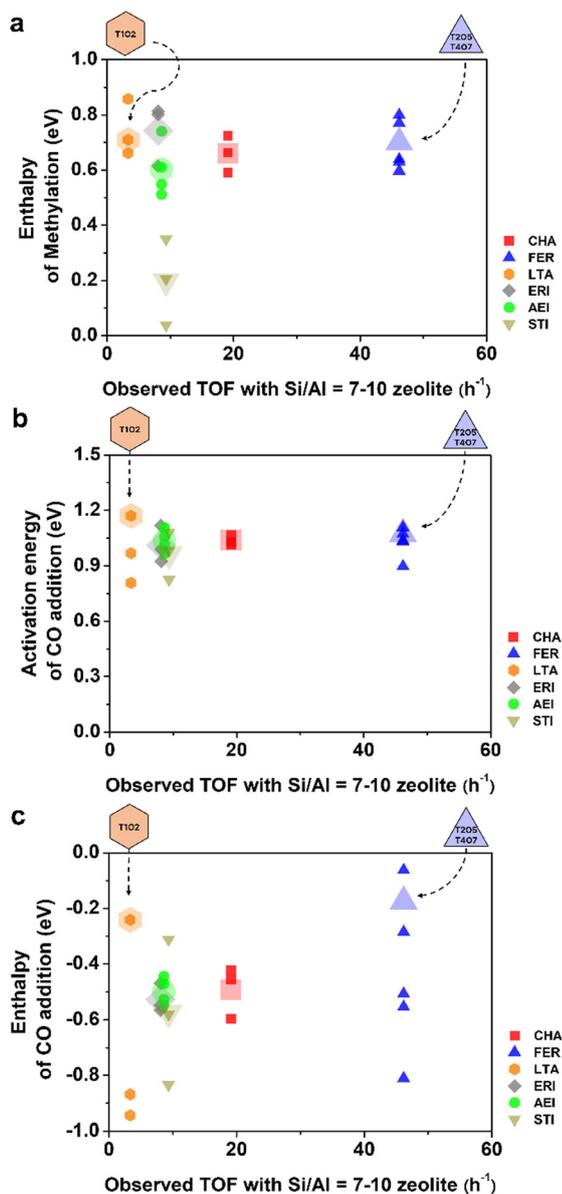
Fig. 5 Correlation between DFT calculated energies with the observed TOF for each zeolite with Si/Al = 7–10 (except for ERI (~5)). (a) Enthalpy of methylation energy; (b) activation energy of CO addition; (c) enthalpy of CO addition.

trend emerges. Therefore, while the DFT results for TxOy sites may be valid for evaluating the reactivity of different TxOy sites within a single topology, they appear insufficient when extended to comparisons across multiple zeolite topologies. Although these calculations consider each framework as a periodic model, the computational approach seems to overlook several critical factors.

2.3 Structural specificity of the TxOy site

Boronat *et al.* identified the T3-O33 site (here referred to as T3O8) in the MOR framework as a key contributor to the high DME carbonylation reactivity, noting that a particular orientation of the SMG is necessary for efficient DME carbonylation within the channel structure.[14] This specific orientation emerges because CO diffuses toward the surface methyl group (SMG), which is formed when a proton at a given TxOy site is replaced, and preferentially attaches orthogonally to the carbon atom of the SMG. The information of the zeolite T and O sites and the orientation of the SMG at each TxOy site is listed in Table S3 with the additional information in Fig. S46–S51 in section S5 of the SI for deeper understanding through graphical illustration. Geometrically, this can be related to the central atom angle ∠OCC of the transient [Z–CH$_3$–CO]‡ complex during the CO addition step, where O refers to the oxygen of the TxOy site that anchors the SMG, the first C is the center carbon of the SMG, and the second C is the carbon of the reacting CO molecule (see Fig. 7). As previously explained with Fig. 2c, the reason MOR shows excellent reactivity is because the reactant gas CO can be easily added to the SMG in the orthogonal direction. Therefore, the closer the ∠OCC is to 180°, where 'nucleophilic backside attack' of CO on the center carbon of SMG readily occurs, the easier it is to form the transient [Z–CH$_3$–CO]‡ complex, so the CO addition activation energy is relatively low, facilitating subsequent reaction steps.[14–16,44,45] Although diffusion effects can influence DME carbonylation at elevated temperatures,[46] the present study was conducted at 165 °C and 2.0 MPa CO, conditions chosen to suppress side reactions and ensure kinetic control by the CO addition step. The observed TOFs thus reflect intrinsic structural effects rather than diffusion or transport limitations.

To determine the ∠OCC bond angle, the DFT calculations at the most stable transition state energy level can be utilized. However, exhaustively evaluating all TxOy sites across the zeolites featured in this study would be computationally expensive. Therefore, we calculated the ∠OCC bond angles, along with the O$_Z$–C$_{SMG}$ and C$_{SMG}$–C$_{CO}$ distances in the transition state (see Fig. 7), for only the effective TxOy sites in each topology along with the associated CO addition activation energies (see Table 3). Here, O$_Z$ represents the zeolite framework oxygen, C$_{SMG}$ refers to the carbon of the surface methoxy group, and C$_{CO}$ refers to the carbon in reacting CO molecule.

The ∠OCC angle of the transient compound [Z–CH$_3$–CO]‡ shows a good correlation with catalytic performance. Several effective TxOy sites in MOR, FER, and CHA—zeolites known for

within the FER framework (the T4O7 site, as identified by Feng *et al.*) is not more advantageous than other T sites within FER in this study. Fig. 5a shows this phenomenon more distinctively, corroborating previous observations.[15]

In conclusion, although lower methylation enthalpy facilitates the framework hydroxyl group in the subsequent CO addition step, it does not serve as a reliable metric for comparing different zeolite topologies. This result also contradicts the explanations given by Feng *et al.* for the performance differences between MOR and FER. Likewise, the DFT calculation of activation energy and enthalpy for the CO addition step fails to account for the significant TOF differences, as shown in Fig. 5b and c, where no discernible
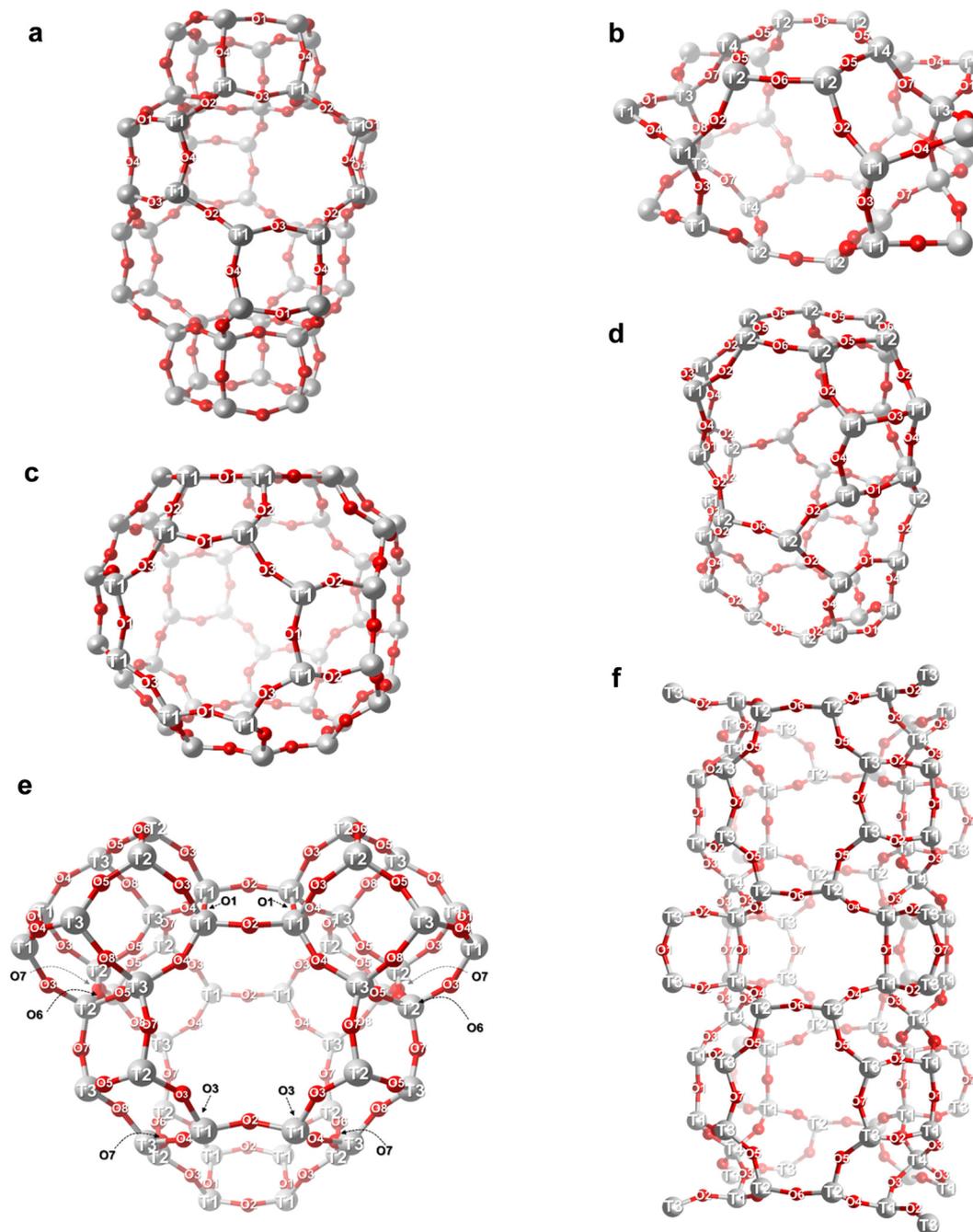
Fig. 6 Detailed TxOy site locations of the zeolites examined in this study. The number of distinct tetrahedral sites (T-sites) and bridging oxygens (O-sites) for each zeolite was determined based on structural data from the IZA database.[23] (a) CHA; (b) FER; (c) LTA; (d) ERI; (e) AEI; (f) STI. [Atom color] gray: tetrahedral site (T-site), red: bridging oxygen.

relatively high reactivity—exhibit an ∠OCC angle close to 180°. A closer inspection reveals that the ∠OCC angle at the MOR T3O8 site (177.8°) is slightly farther from 180° than that at the FER T4O7 site (179.5°). Nevertheless, MOR is widely known to exhibit much higher reactivity than FER (although with rapid deactivation). This discrepancy implies that reactivity cannot be fully explained by the bond angle of the transient complex alone. The ∠OCC angle becomes even more pivotal when comparing zeolites with

3-dimensional pore networks. For instance, the notably higher reactivity of CHA compared to the other 3-dimensional pore-type zeolites (such as LTA, ERI, and AEI) can be partly attributed to the ∠OCC angle (177.8°) at the CHA T1O2 site. Zeolites with 8-MR TxOy sites with ∠OCC angles below 177° exhibit significantly lower TOFs than CHA, as seen in Fig. 3b.

Moreover, as the Brønsted acid site (BAS) occupancy at a TxOy site rises, where the ∠OCC angle is around 180°, the
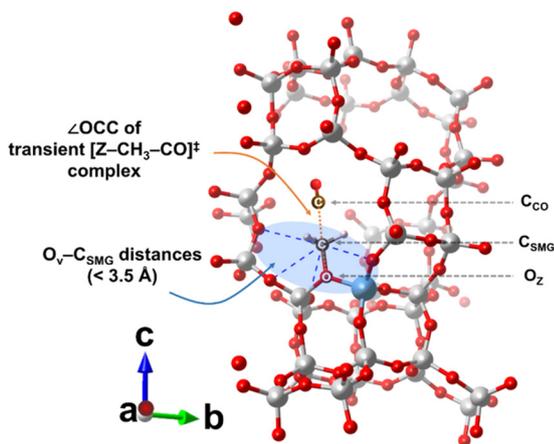
Fig. 7 Geometric configuration of a transient $[Z–CH_3–CO]^{\ddagger}$ complex with nucleophilic backside attack of CO on the surface methyl group (SMG) substituted for the Brønsted acid site on T1O3 in CHA. The $\angle OCC$ ($\angle O_Z–C_{SMG}–C_{CO}$) of the transient complex and the $O_V–C_{SMG}$ distance (<3.5 Å) are highlighted in orange and blue, respectively. [Atom color] brown: carbon, pink: hydrogen, gray: silicon, cyan: aluminum, red: oxygen.

validity of the association between this angle descriptor and reactivity can be clarified. While the distribution of BASs is likely influenced by the synthesis procedure of each zeolite, the exact nature of this relationship remains unclear and even varies across zeolite types. This site preference is mainly discussed in SI section S1 about criteria for selecting effective Brønsted acid sites for DFT. A precise measurement of proton preference at each $TxOy$ site would be ideal but remains challenging due to the myriad of environmental factors (*e.g.*, reaction temperature, calcination, and pretreatment) affecting the sample. In zeolites with multiple crystallographically unique T sites, such as FER and STI, even state-of-the-art computational techniques demand substantial resources for accurate analysis. Consequently, prior studies have generally provided only approximate estimates of BAS preferences in diverse zeolite topologies.[38,47–55] Accordingly, this study presents relative occupancy levels of effective $TxOy$ sites instead of exact distribution, thereby underscoring the usefulness of the $\angle OCC$ angle as a key descriptor for assessing reactivity.

In the case of CHA, at high Si/Al ratios, most protons occupy the T1O1 site. However, as Al substitution for tetrahedral Si increases, protons gradually populate the T1O2 site, which has an $\angle OCC$ angle of 177.8°, favorable for CO addition. Likewise, the proton occupancy in FER is predominantly concentrated at the T4O7 site ($\angle OCC = 179.5°$), facilitating the attack of CO on the methoxy group at this site. On the other hand, for LTA, most protons prefer the T1O2 site, which has an $\angle OCC$ angle of 170.1°, the third lowest among the effective $TxOy$ sites listed in Table 3. While LTA possesses the T1O3 site with a more favorable $\angle OCC$ angle of 176.7° for CO addition, the lowest TOF of LTA among the zeolites studied can be adequately explained by the relative scarcity of proton occupancy at T1O3. In conclusion, if a substantial proportion of actual BASs occupy

the $TxOy$ site with an $\angle OCC$ angle favorable for CO addition, high catalytic performance can be linked more directly to these geometric factors.

The case of ERI is also well explained by this correlation. Previous studies[38,55] indicate that low-silica ERI prefers Al substitution at T2 sites (T2O2 and T2O6), which together contribute 75% of the 8-MR $TxOy$ sites. With $\angle OCC$ angles of 175.6° and 176.3°, these T2 sites favor CO addition and suggest that ERI could be relatively reactive among other small-pore zeolites. However, experimentally verifying this has been challenging due to difficulties in synthesizing high-silica ERI with Si/Al > 10. Hence, limited reaction data exist for ERI to confirm this conclusion. Nonetheless, as can be seen from Fig. 3b, with a Si/Al ratio of 5, ERI exhibits slightly higher reactivity than AEI, STI, and LTA with Si/Al ratios of 7–8. This trend suggests that ERI likely surpasses other small-pore zeolites in reactivity, supporting the notion that ERI has promising characteristics for DME carbonylation.

For AEI, prior research does not specify a $TxOy$ site preference for Brønsted acid sites; however, each 8-MR $TxOy$ site in AEI exhibits an $\angle OCC$ angle of 175° or lower, which is somewhat suboptimal for CO addition. This observation explains the comparatively lower TOF of AEI than CHA, even though the two zeolites differ only in their stacking order of double-6-ring (d6r) units. By contrast, this geometric metric does not fully account for the notably low TOF of STI. The $\angle OCC$ angles for T2O5 and T3O7 sites within the 8-MR of STI are 175.1° and 176.5°, respectively. Although these angles are not ideal (180°) for CO addition *via* 'nucleophilic backside attack' on the SMG, these angles should not severely hinder CO addition. However, Fig. 3b indicates that the TOF of STI is nearly the same as that of AEI, suggesting similarly low reactivity. Despite prior expectations, which are based on the relatively low methylation energy and CO addition activation energy of STI, that STI would outperform other reference zeolites, experimental findings show otherwise. This discrepancy indicates that factors beyond the $\angle OCC$ angle or DFT-calculated values for specific $TxOy$ sites must be considered to fully account for the reactivity differences.

Additionally, examining the $O_Z–C_{SMG}$ and $C_{SMG}–C_{CO}$ distances for each $TxOy$ site reveals that they are mostly around 2 Å, showing no significant variation. Because the CO addition step occurs in the narrowly confined zeolite pore spaces, evaluating which $TxOy$ site better stabilizes the transient compound $[Z–CH_3–CO]^{\ddagger}$ cannot rely solely on these distance metrics. Rather, effective stabilization of the $[Z–CH_3–CO]^{\ddagger}$ charge density is crucial for facilitating CO addition. Oxygen atoms within *ca.* 3.5 Å of the central carbon of SMGs have the greatest impact on its transition-state stabilization, as they readily donate electrons through delocalization. Consequently, the proximity of the central carbon of SMGs to nearby framework oxygens has a more pronounced influence on reactivity than simple interatomic distances within the transient compounds. To quantify these effects, we introduced the descriptor $N_{O,CC}$, defined as the number of vicinal framework oxygens (O_V) within 3.5 Å of C_{SMG}, along with the average O_V–
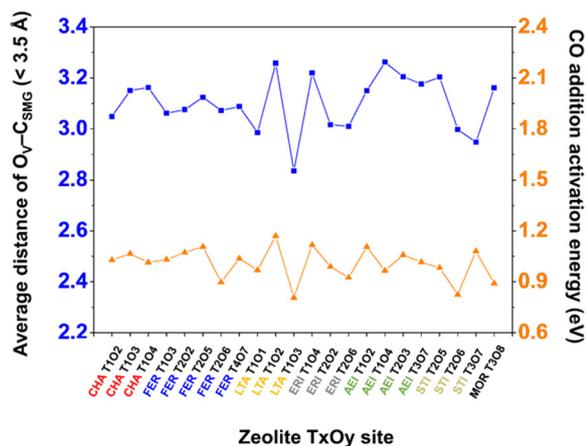
Fig. 8 Average $O_V–C_{SMG}$ distance (<3.5 Å) and CO addition activation energy at effective TxOy sites of selected zeolites.

C_{SMG} distance. These values for each TxOy site in each topology are listed in Table 3.

Fig. 8 shows that the average $O_V–C_{SMG}$ distance (<3.5 Å) correlates reasonably with the CO addition activation energy identified in section 2.2. Although some differences exist in the details, the overall similarity suggests that the stabilization of CO addition activation energy is largely influenced by close-contact oxygen atoms. These minor differences may stem from using an averaged $O_V–C_{SMG}$ distance, which does not fully distinguish between oxygens directly adjacent to the Al site and those slightly farther away.[16] Nevertheless, it is clear that the DFT calculation results presented in section 2.2 are not fully aligned, or proportional with the TOF trends shown in Fig. 3b. Overall, the observed discrepancy between the CO addition activation energies and average $O_V–C_{SMG}$ distances among different TxOy sites reflects the limitations in applying simple geometrical descriptors in predicting catalytic performance.

Those outcomes in section 2.2–2.3 suggested that conventional approaches, which are relying on examining only one effective TxOy site in isolation and investigating a single active TxOy site as the sole determinant of reactivity, are insufficient to explain the reactivity variation among zeolites. This underscores the necessity in building better descriptors that capture the multi-faceted, complex nature in zeolite reactivity, as addressed in the following sections.

2.4 Channel dimensionality of zeolite topology

As detailed in section 1 on the DME carbonylation mechanism (eqn (1)–(4)), the surface acetyl group (SAG) created during the CO addition step ultimately forms the final product, MA, through DME adsorption. During this esterification process, the adsorbed MA leaves the BAS, which is then re-substituted by a SMG. It is worth noting that DME not only creates the active methyl group, which is known as the most abundant reaction intermediate (MARI), but also participates in the esterification that follows CO addition. Even if the partial pressure of DME is relatively low, it still sufficiently saturates the BAS of the zeolite

to maintain a continuous supply of SMGs, thus sustaining the reaction cycle.[17,33,56,57] Meanwhile, the high CO partial pressure (*ca.* 1.8 MPa) further increases the rate of reaction. This mechanism implies that, once formed, the SMG will not necessarily remain on a single acid site; instead, it may migrate to other sites during the esterification, driven by CO addition, a phenomenon sometimes called as "remethylation". Thus, the average distance between BASs (for example, estimated by the ratio of accessible volume to the number of BASs) likely contributes significantly to overall reactivity of DME carbonylation.

Based on this insight, we propose the descriptor, "molecule adsorption isovolume.". In Fig. 9a, the gray and cyan regions depict the volumetric zones where critical portions of the reaction, especially interactions at BASs, predominantly occur within each zeolite, determined using helium (He) and CO as internal probe molecules, respectively. The isovolume region extends beyond the sum of the kinetic diameter of each probe molecule and the characteristic van der Waals radius (1.35 Å) of the framework atoms (oxygens), thereby defining where these probe molecules can diffuse and where the reaction takes place. This descriptor serves as a precise method for analyzing how active sites are distributed.

The isovolume is calculated exclusively on the basis of van der Waals radii, eliminating the effect of external energy that can promote molecular diffusion *via* vibration and rotation (*i.e.*, hard-sphere model). To address this limitation under a controllable criterion, He, which is one of the smallest probe molecules, with a kinetic diameter of 2.60 Å, was employed to calculate the "He isovolume" (light gray). The cyan zone represents the CO-accessible volume, highlighting regions where DME carbonylation can occur *via* CO addition. Table 4 summarizes the numerical values of the corresponding isovolumes (V_{He} and V_{CO}) shown in Fig. 9a.

Channel dimensionality can be assessed directly by examining isovolume data graphically. Although all zeolites in this study share an 8-MR pore system, they differ fundamentally in properties such as unit cell shape and channel dimensionality. Among these, CHA, LTA, ERI, and AEI are classified as 3-dimensional frameworks; each contains a repeating cage structure that connected with six neighboring cages through 8-MR pores, forming an interconnected 3-dimensional network. The isovolume values for these 3-dimensional type zeolites are calculated based on their cage structures.

In contrast, MOR and FER stand out for their distinct 2-dimensional frameworks, which many previous studies have linked to their superior performance. This enhanced reactivity stems from this cross-connected channel structure, where two intersecting channels of different diameters operate synergistically.[12–15,18–21,32,33,58,59] The effectiveness of these channel systems lies in their "role division structure": t-dah (natural tiling of MOR) or t-fer (natural tiling of FER) as the primary active site, while the larger channel promotes smooth product diffusion.

Further evidence for this phenomenon comes from Monte Carlo and dynamic diffusion simulations, which measure CO
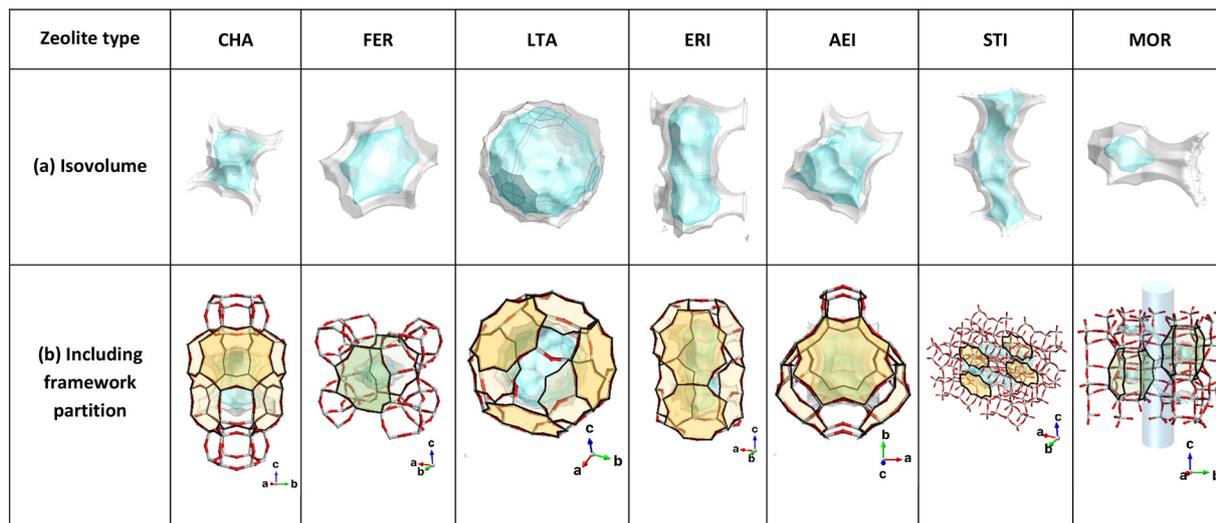
Fig. 9 (a) Graphical data of isovolume where a probe molecule can diffuse into the zeolite framework considering the van der Waals radius of framework molecules and probe molecule. [Color] gray: helium isovolume region, cyan: CO isovolume region; (b) graphical data of the isovolume with framework partition in which the DME carbonylation reaction would prevalently occur. In each framework, the 8-MR pores are highlighted with bold outlines and color shading. All 8-MR pores are colored yellow, except for the FER cage in t-fer and t-dah of MOR, which are highlighted with green boxes. [Isovolume color] light gray: tetrahedral site (where Si or Al would be located), red: bridging oxygen.

aggregation and MA transport, enabling systematic comparisons across various zeolite types.[59,60] Nevertheless, these computational studies often exhibit certain limitations, such as overlooking the actual distribution of BASs (particularly those that dominate in real zeolites) and not explicitly applying the DME carbonylation mechanism at those sites. Relying predominantly on computational predictions over empirical reaction data may thus result in incomplete conclusions.

The isovolume graphical data also reveal notable structural distinctions between FER and MOR shown in Fig. 9b. Using CO as a probe molecule, a small cage (highlighted in cyan) appears within the FER cage (part of t-fer) and t-dah (MOR) natural tilings (green-colored box) whereas using helium as a probe uncovers staggered interconnections in MOR, depicted in gray fin-like shape. This distinctive 8-MR side-pocket structure helps clarify why the CO addition at the MOR T3O8 site is particularly favorable (see also Fig. 2c).

This side-pocket runs parallel to the c-axis (see Fig. 9b MOR, light blue-colored cylinder). Although its diameter (~5.5 Å) is somewhat narrow for MA, it allows the CH_3^+ (methyl cation) released from DME during esterification to traverse the pocket. Thus, the T3O8-site-rich side pocket offers a short diffusion path for methyl groups to be rapidly substituted. Moreover, the favorable OCC angle (177.8°) supports surface acetyl group (SAG) formation through CO addition at the acid site, contributing to the higher reactivity of MOR compared to FER.

MA, the final product of DME carbonylation, can then diffuse through the main 12-MR channel, creating a well-defined role division structure that promotes overall reactivity. However, this structure also has a drawback: when acid sites are distributed in large channels like the 12-MR, dehydrogenation

can occur, producing hydrocarbons that hinder MA diffusion, accelerate coking, and degrade catalyst performance.

STI, although structurally classified as a 2-dimensional zeolite, is widely recognized as functionally 1-dimensional in terms of molecular diffusion behavior. This transport confinement holds for most molecules involved in chemical reactions, including CO, which serves as the probe molecule in the cyan isovolume shown in Fig. 9. In STI, the primary 10-MR channels are linked through 8-MR pores, yet it lacks the role division structure (such as t-fer of FER or t-dah of MOR) found in the 2-dimensional zeolites MOR and FER. Because STI lacks the repeating cage structure found in cage-type zeolites (e.g., CHA, AEI, ERI, etc.), the unit cell volume was used to calculate its repeating structural unit; this shape is also depicted in Fig. 9a.

Although the specific approach to isovolume-based dimensional classification may differ, we ultimately assume a minimum repeating unit of a 3-dimensional structure for each topology in this study. Given the focus on the DME carbonylation mechanism, particular attention is paid to the effective TxOy sites contributing to the reaction. Accordingly, the isovolume concept aims to show how narrower internal volume (where reactions occur) and a higher density of BASs within that volume can result in proportionally higher TOF. This correlation provides a quantitative measure of how readily BASs can migrate across the other sites, reflecting the frequency of the DME carbonylation cycle.

Table 4 lists the values needed to calculate these frequencies, including He and CO isovolumes (V_{He} and V_{CO}), the number of isovolumes per unit cell (N_I) for each topology, and the count of effective oxygen sites (N_{EO}) critical to the reaction. Oxygen-site numbering follows the IZA database[23] and the criteria for selecting effective oxygen sites across tested zeolites are given in

SI section S1. We define three descriptors (D_{He}, D_{CO}, and D_F) as follows:

$$D_{He} = 100 \frac{N_{EO}}{N_I V_{He}} \tag{5}$$

$$D_{CO} = 100 \frac{N_{EO}}{N_I V_{CO}} \tag{6}$$

$$D_F = \sqrt{D_{He} D_{CO}} \tag{7}$$

Following the reasoning outlined earlier in this section, D_{He} numerically depicts the density of effective oxygen sites within the He isovolume per unit cell and D_{CO} characterizes their distribution within the CO isovolume. The descriptor D_F is the geometric mean of these two numbers.

Fig. 10 shows the values of D_{He}, D_{CO}, and D_F for each topology, corresponding to the observed TOFs for samples with Si/Al ratios of 7–10 (the appropriate Si/Al ratio range that allows comparison between different zeolite topologies in this study). The graphs include trend lines for data both excluding MOR (solid line) and including MOR (dashed line), along with associated R^2 values or slope standard error (SSE) values.

Fig. 10a and b show a linear correlation for the 8-MR zeolites (excluding MOR). However, when MOR data are included, the R^2 value for D_{He} decreases from 0.96 to 0.91, and the SSE for D_{CO} increases from 0.10 to 0.12. These changes suggest that D_{He} and D_{CO} alone cannot fully capture the behavior of MOR, with its 8-MR side pocket and unique internal channel structure.

In contrast, Fig. 10c shows that using D_F as a descriptor reveals a more robust linear correlation with TOF, even when MOR is included (R^2 increases 0.96 to 0.98, SSE decreases from 0.07 to 0.04). These findings underscore the importance of considering V_{He} and V_{CO} isovolumes when analyzing reactivity. They significantly support the notion that, in addition to CO addition, the "remethylation" step during subsequent esterification critically influences catalytic performance.

In conclusion, previously proposed descriptors for local BASs have shown limitation in explaining the reactivity differences across various zeolites. However, once the essential elementary steps in the reaction mechanism are clearly identified, it becomes possible to derive a 3-dimensional structural descriptor that strongly correlates with catalytic performance, based solely on the intrinsic framework geometry without the need for extensive computational analysis.

3 Conclusions

It is widely accepted that investigating the influence of 8-MR zeolites on DME carbonylation requires both thorough experimental and theoretical approaches. In this study, we systematically investigated multiple 8-MR zeolites and proposed a universal descriptor that captures the correlation between zeolite structure and DME carbonylation reactivity. It is emphasized that the findings of this work clearly indicate that conventional parameters, such as DFT-calculated energies of RDSs (CO addition and methylation steps), and local geometric
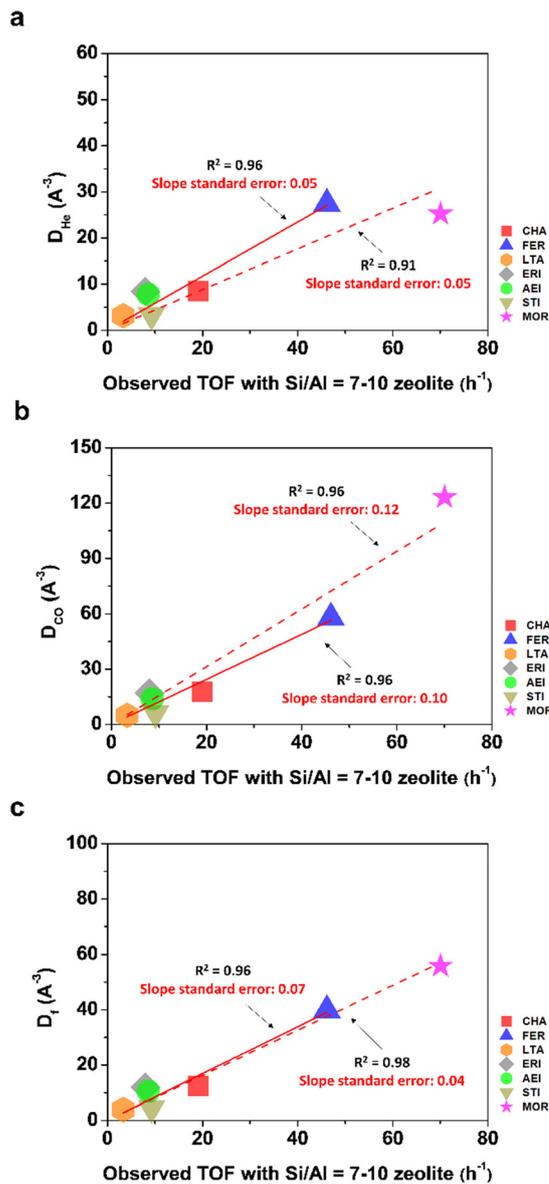

Fig. 10 Correlation between 3-dimensional descriptors with observed TOF for each zeolite with Si/Al = 7–10 (except for ERI (~5)). (a) D_{He}, (b) D_{CO}, and (c) D_F. To examine the structure–reactivity correlation, linear regression was performed for the topologies excluding MOR and for those including MOR. The results are represented as a solid line and a dashed line, respectively.

descriptors of the transition state (*e.g.*, ∠OCC angle or average distance of O_V–$C_{SMG} < 3.5$ Å), fully capture the noticeable variations in TOF resulting from different topologies.

It should be noted that these conventional approaches were confined to evaluating the contribution of individual TxOy sites, rather than considering the broader 3-dimensional configuration of the zeolites. In order to fill this gap, we introduced two structural descriptors, D_{He} and D_{CO}, which quantify how many effective oxygen sites exist within pre-defined isovolumes (V_{He} and V_{CO}) linked to key steps in DME carbonylation. By using He as a probe for methyl cation pathways and CO as a probe for the CO addition pathway, each descriptor captures unique yet

complementary information on the catalysts' internal environment. We highlight that each descriptor (D_{He} and D_{CO}) shows strong correlation with TOF across multiple 8-MR zeolites, and taking their geometric mean (D_F) gives an even better correlation, especially when MOR is included.

We underscore that this observation demonstrates the prominence of CO addition and remethylation steps in controlling DME carbonylation reactivity, given that the proposed descriptor D_F explicitly includes both V_{He} and V_{CO}, representing the two key steps, respectively. These results highlight two primary insights. First, zeolite structure and reactivity cannot be captured by focusing solely on local descriptors within the framework. Nonetheless, detailed investigation of DFT-calculated energies, interatomic distances, and conformation angles of the transition state remain critical, as they help define the three-dimensional isovolume more systematically for explaining reactions based on the zeolite framework and pore structures.

It should also be noted that D_F was constructed based on the mechanistic features of DME carbonylation. Although the concept may be extendable, its applicability to other 8-MR reactions has not been validated and should be examined in future studies. Finally, the considerations of this work may advance the foundation for zeolite catalyst design by relating reactivity to 3-dimensional structural descriptors, providing both theoretical insights and practical guidance for optimizing performance in commercial applications.

4 Experimental

4.1 Synthesis

Complete details of the zeolite synthesis methods are detailed in section S2 of the SI.

4.2 Characterization

Powder X-ray diffraction (PXRD) patterns were examined for each zeolite sample on a SMARTLAB X-ray diffractometer using Cu Kα radiation in the range of 2θ from 5° to 40° to confirm the crystallinity of the zeolites.

NH$_3$-temperature-programmed desorption (NH$_3$-TPD) was conducted with a BELCAT-M instrument to examine the total Brønsted acid site (BAS) concentration. Prior to the main TPD analysis, the sample (~50 mg) was pretreated under a flow of He (30 ml min^{-1}) at 500 °C for 1 h. Then, the sample was cooled to 100 °C, after which NH$_3$ was adsorbed for 1 h. Subsequently, the sample was heated from 100 to 800 °C at a ramping rate of 10 °C min^{-1}, and the TCD signals were simultaneously acquired. The resulting profiles were deconvoluted into three Gaussian peaks, which can be typically interpreted respectively as weak, moderate, and strong acid sites. The higher the temperature of ammonia desorption, the stronger the acid sites. Generally, the weak and moderate acid sites are considered as Lewis acid sites or defected acid sites from extra-framework species in the zeolite. On the other hand, the strong acid sites are normally assigned to BASs.

Fourier-transform infrared spectroscopy (FT-IR) analysis was conducted on a PerkinElmer Frontier with a liquid N$_2$-cooled mercury–cadmium-telluride (MCT) detector to measure Brønsted and Lewis acid sites distributed on a larger than 10-membered ring (10-MR) framework of the MOR and FER through an *in situ* adsorption of pyridine probe molecules. In more detail, the sample was pretreated at 500 °C for 1 h under a N$_2$ flow and cooled down to 165 °C by measuring the respective background spectra. After the adsorption of probe pyridine for 1 h, the physisorbed surface pyridine was removed under vacuum conditions for 30 minutes, and the Py-IR spectra were obtained at the desorption temperature of 165 °C.

The results of characterization, calculated energy diagrams, framework geometries of the surface methyl group (SMG) for the TxOy sites of the investigated zeolites are listed in SI section S3.

4.3 Reaction and activity measurement

The gas-phase DME carbonylation reaction was evaluated by using a fixed-bed tubular reactor with an inner diameter of 7 mm. Before the carbonylation test, 0.3 g of each zeolite sample was pretreated under an N$_2$ flow to remove any contaminants at 1 bar and 500 °C at a ramping rate of 10 °C min^{-1} for 1 h. Following pretreatment, the main reaction test was conducted at 165 °C and 2.0 MPa, with a space velocity (SV) of 2000 L kg$_{cat}$$^{-1}$ h^{-1} and a feed consisting of DME/CO/N$_2$ = 4.5/90/5.5 vol%. The effluent stream was analyzed online by using a gas chromatograph (Younglin GC, YL6100) with a flame ionization detector (FID) and an HP-PLOT-U capillary column to identify and quantify DME, methanol (CH$_3$OH), methyl acetate (MA), and other light hydrocarbons.

Comprehensive numerical values for reactivity, 8-MR BAS density, and the essential rings and channel dimensions[23] relevant to each topology are listed in Table 1.

4.4 Computational methods for DFT calculations

Density functional theory (DFT) calculations were performed to validate the reaction enthalpies and activation energies for the key steps—methylation and CO addition—in DME carbonylation at various BASs within small-pore zeolite frameworks. The choice of BASs was informed by representative studies identifying locations where these sites are most densely populated.

The VASP code, GGA-PBE XC-functionals, and zero damping D3-Grimme's correction for van der Waals dispersion are employed for the computation.[61] A cutoff energy of 400 eV was used, and all structures are relaxed.[62–64] The coordinates of reagents and products were optimized until the maximum force on each atom was below 0.05 eV Å^{-1},[65,66] and the energy was converged to within a 1×10^{-6} eV threshold. Transition states were initially located *via* the NEB method, using a convergence criterion of 0.3 eV Å^{-1},[67,68] and then refined with the dimer method, which reached a force convergence of 0.05 eV Å^{-1}.[69] During the dimer method, only the CH$_3$CO$^+$ moiety was relaxed.

Table 1 Characterization data and catalytic performances of zeolites having small pores (8MR)

Catalysts[a]	8-MR Brønsted acid site density[b] (mmol g^{-1})	Essential rings[c]	Channel dimensionality	MA generation rate, SS[e] (mol kg$_{cat}^{-1}$ h^{-1})	TOF, SS[e] (h^{-1})
CHA (5.1)	0.864	$[8_1 \cdot 6_1 \cdot 4_2]$	3-Dimensional	8.0	9.2
CHA (7.2)	0.822			15.7	19.1
CHA (12.7)	1.314			19.6	14.9
CHA (19.8)	1.346			13.4	10.0
CHA (25.9)	1.030			8.7	8.4
CHA (50.8)	0.416			2.1	5.2
CHA (67.5)	0.333			1.3	4.1
CHA (79.5)	0.231			0.7	3.1
FER (8.2)	0.914	$[10_1 \cdot 8_1 \cdot 6_1 \cdot 5_4]$	2-Dimensional	32.8	35.9
FER (10.0)	0.498			28.1	56.5
FER (15.4)	0.213			12.7	59.5
FER (17.3)	0.229			8.6	37.7
LTA (8.1)	0.694	$[8_1 \cdot 6_1 \cdot 4_2]$	3-Dimensional	2.3	3.4
LTA (17.8)	0.544			3.5	2.6
LTA (26.8)	0.368			1.4	3.7
LTA (44.0)	0.189			0.5	2.4
ERI (~5)	0.819	$[8_1 \cdot 6_3 \cdot 4_2]$	3-Dimensional	6.6	8.0
AEI (7.0)	1.389	$[8_2 \cdot 6_1 \cdot 4_4]$	3-Dimensional	9.6	6.9
AEI (10.0)	1.394			14.4	10.3
STI (7.8)	0.956	$[10_1 \cdot 8_2 \cdot 6_1 \cdot 5_1 \cdot 4_2]^d$	Functionally[d]	6.8	7.1
STI (9.9)	0.448		1-Dimensional	5.2	11.6
CMOR (10.0)	1.369	$[12_1 \cdot 8_3 \cdot 5_5 \cdot 4_1]$	2-Dimensional	96.0	70.1

[a] The number in parentheses indicates the Si/Al ratio. All tested catalysts fall within the range of Si/Al ratios that are feasible for synthesis. [b] The 8-MR Brønsted acid site (BAS) density was calculated by using an NH$_3$-TPD curve, which was deconvoluted by Gaussian distribution using a 3-distribution model (GN(DLS) method) with damping set at 0.7. Among the 3 deconvoluted peaks, the peak in the highest temperature range distribution was chosen to represent the 8-MR BAS.[25–31] Pyridine-IR was also used to estimate the Brønsted acid sites that can be adsorbed in the channel larger than 8-MR, consisting of FER and MOR, especially in this study. In these cases, the 8-MR BAS density was calculated by subtracting the BAS density derived by pyridine-IR from the strong acid site density estimated by NH$_3$-TPD. [c] Essential rings, derived from face symbols of natural tiles, are 'strong' rings that cannot be reduced to sums of smaller rings, distinguishing them as key structural elements in zeolite channels.[23] [d] In STI, 8-MR pores connect parallel 10-MR channels, which are oriented in the [100] direction, but when CO is used as a probe molecule, van der Waals forces can cause the 8-MR pores to pucker, blocking the connection between the 10-MR channel (see SI section S1-STI). [e] Approximation to steady state (SS), which is the average value in the range of 30–34 h. However, CHA (79.5) is an exception, showing low reactivity, and is represented as an average value corresponding to the range of 24–28 h.

Table 2 DFT calculated energies of methylation and the CO addition process

Zeolite	Site	Methylation		CO addition	
		ΔE (eV)	Average ΔE (eV)	E_a (eV)	ΔE (eV)
CHA	T1O2	0.590	0.659	1.028	−0.422
	T1O3	0.725		1.065	−0.597
	T1O4	0.663		1.014	−0.456
FER	T1O3	0.638	0.686	1.031	−0.507
	T2O2	0.596		1.072	−0.554
	T2O5[a]	0.629		1.106	−0.063
	T2O6	0.799		0.897	−0.811
	T4O7[a]	0.770		1.037	−0.286
LTA	T1O1	0.661	0.742	0.968	−0.868
	T1O2[a]	0.709		1.169	−0.242
	T1O3	0.857		0.807	−0.944
ERI	T1O4	0.613	0.742	1.116	−0.468
	T2O2	0.812		0.989	−0.547
	T2O6	0.801		0.924	−0.565
AEI	T1O2	0.610	0.602	1.105	−0.445
	T1O4	0.740		0.965	−0.527
	T2O3	0.548		1.057	−0.547
	T3O7	0.511		1.015	−0.471
STI	T2O5	0.350	0.198	0.982	−0.580
	T2O6	0.206		0.825	−0.834
	T3O7	0.038		1.080	−0.312
MOR	T3O8[b]	−0.247	—	0.890	−0.442

[a] Some TxOy sites that are not present in 8-MR but required for discussion. See SI section S1. [b] MOR T3O8 site is introduced in this paper due to its unique site position in mordenite for the selective DME carbonylation process.

Table 3 Geometric descriptors and the derivatives of the transient compound [Z–CH$_3$–CO]$‡$ during the CO addition step for the investigated TxOy sites of each zeolite

| Zeolite | Site | [Z–CH$_3$–CO]$‡$ | | | N$_{O,CC}$ | Average distance of O$_V$–C$_{SMG}$ (<3.5 Å) |
		∠OCC (°)	O$_Z$–C$_{SMG}$ (Å)	C$_{SMG}$–C$_{CO}$ (Å)		
CHA	T1O2	177.8	2.024	1.989	3	3.049
	T1O3	172.3	2.028	2.018	4	3.151
	T1O4	175.5	2.012	2.007	4	3.163
FER	T1O3	171.3	2.034	1.975	3	3.062
	T2O2	134.8	2.035	1.995	3	3.076
	T2O5^a	174.7	2.034	1.968	4	3.125
	T2O6	171.5	2.011	1.999	4	3.073
	T4O7^a	179.5	2.023	1.998	3	3.088
LTA	T1O1	172.9	2.015	2.013	3	2.986
	T1O2^a	170.1	2.004	1.966	6	3.258
	T1O3	176.7	2.022	2.031	2	2.835
ERI	T1O4	172.1	2.004	1.990	4	3.220
	T2O2	175.6	2.022	2.010	3	3.017
	T2O6	176.3	2.031	2.001	4	3.011
AEI	T1O2	172.5	2.026	1.965	4	3.150
	T1O4	174.6	2.030	1.980	4	3.263
	T2O3	174.4	2.002	1.956	4	3.206
	T3O7	172.1	1.989	1.952	4	3.177
STI	T2O5	175.1	2.016	1.953	5	3.204
	T2O6	169.5	2.031	2.043	4	2.998
	T3O7	176.5	2.041	2.014	2	2.948
MOR	T3O8^b	177.8	2.009	2.003	4	3.162

^{a} Some TxOy sites that are not present in 8-MR but required for discussion. See SI section S1. ^{b} MOR T3O8 site is introduced in this paper due to its unique site position in mordenite for selective DME carbonylation process.

Table 4 The information of the effective oxygen site and parameters that are needed for calculation of 3-dimensional descriptors (D_{He}, D_{CO}, and D_F). The V_{He} and V_{CO} were derived from two different probe molecules, helium and carbon monoxide for each investigated 8-MR zeolite

Zeolite type	Number of T site per unit cell	V_{He} (Å^3)	V_{CO} (Å^3)	Effective oxygen site	N_I	N_{EO}	D_{He} (Å^{-3})	D_{CO} (Å^{-3})	D_F (Å^{-3})
CHA	36	210.7	102.2	O2, O3, O4	3	54	8.54	17.6	12.3
FER	36	80.4	38.0	O2, O3, O5, O6, O7	2	44	27.4	58.0	39.8
LTA	24	385.8	246.6	O1, O3, (O2)	1	36	9.33 (3.11)^a	14.6 (4.87)^a	3.89
ERI	36	250.5	124.0	O2, O4, O6	2	42	8.38	16.9	11.9
AEI	48	179.3	101.0	O2, O3, O4, O7	4	56	7.81	13.9	10.4
STI	72	246.5	133.6	O5, O6, O7	4	32	3.25	5.99	4.41
MOR	48	111.0	22.7	O2, O3, O5, O7, O8, O10	2	56	25.2	123	55.8

^{a} Similar to other zeolites, the effective oxygen sites of the LTA-type framework (those contributing to the reaction) are located on the 8-MR. However, during synthesis, these sites predominantly occupy the O2 site on the d6r unit. Therefore, values corresponding to actual cases are indicated in parentheses for clarity. See SI section S1.

All DFT calculations were carried out under a static framework approximation at 0 K, without including thermal vibrations or dynamic solvent effects. While our calculations neglect finite-temperature effects and vibrational dynamics, this static DFT approach is commonly used and sufficient for capturing qualitative trends in zeolite-catalyzed reactions.

Author contributions

D. J. Jeong: conceptualization, writing – original draft, review, editing and visualization, design experimental work, zeolite synthesis, data analysis, characterization, reaction and calculation of 3-dimension related data. X. Wang: data analysis, characterization, reaction. N. Park: DFT calculation. D. Lee: zeolite synthesis. Y. Lee: figuration of the DFT energy diagram in the SI. J. W. Bae: writing – review & editing, supervision. W. B. Lee: writing – review & editing, supervision. J. H. Kang: writing – review & editing, supervision, conceptualization. D. J. Jeong, X. W., and N. P. contributed equally to this work.

Conflicts of interest

There are no conflicts to declare.

Data availability

The data supporting this article have been included in the main text and as part of the supporting information (SI). Any further details will be available upon request. Supplementary

References

1 P. Kalck, C. Le Berre and P. Serp, Recent advances in the methanol carbonylation reaction into acetic acid, *Coord. Chem. Rev.*, 2020, **402**, 213078.

2 P. Pal and J. Nayak, Acetic acid production and purification: Critical review towards process intensification, *Sep. Purif. Rev.*, 2017, **46**, 44–61.

3 S. K. Bhatia and Y. H. Yang, Microbial production of volatile fatty acids: Current status and future perspectives, *Rev. Environ. Sci. Bio/Technol.*, 2017, **16**, 327–345.

4 N. Yoneda, S. Kusano, M. Yasui, P. Pujado and S. Wilcher, Recent advances in processes and catalysts for the production of acetic acid, *Appl. Catal., A*, 2001, **221**, 253–265.

5 P. M. Maitlis, A. Haynes, G. J. Sunley and M. J. Howard, Methanol carbonylation revisited: Thirty years on, *J. Chem. Soc., Dalton Trans.*, 1996, 2187–2196.

6 A. Haynes, in *Advances in Catalysis*, ed. B. C. Gates and H. Knözinger, Elsevier, Amsterdam, 2010, ch. 1, vol. 53, pp. 1–45.

7 C. M. Thomas and G. Süss-Fink, Ligand effects in the rhodium-catalyzed carbonylation of methanol, *Coord. Chem. Rev.*, 2003, **243**, 125–142.

8 P. Cheung, A. Bhan, G. J. Sunley and E. Iglesia, Selective carbonylation of dimethyl ether to methyl acetate catalyzed by acidic zeolites, *Angew. Chem., Int. Ed.*, 2006, **45**, 1617–1620.

9 D. Mao, W. Yang, J. Xia, B. Zhang, Q. Song and Q. Chen, Highly effective hybrid catalyst for the direct synthesis of dimethyl ether from syngas with magnesium oxide-modified HZSM-5 as a dehydration component, *J. Catal.*, 2005, **230**, 140–149.

10 T. Pöpken, L. Götze and J. Gmehling, Reaction kinetics and chemical equilibrium of homogeneously and heterogeneously catalyzed acetic acid esterification with methanol and methyl acetate hydrolysis, *Ind. Eng. Chem. Res.*, 2000, **39**, 2601–2611.

11 H. Ham, H. S. Jung, H. S. Kim, J. Kim, S. J. Cho, W. B. Lee, M. J. Park and J. W. Bae, Gas-phase carbonylation of dimethyl ether on the stable seed-derived ferrierite, *ACS Catal.*, 2020, **10**, 5135–5146.

12 A. Bhan, A. D. Allian, G. J. Sunley, D. J. Law and E. Iglesia, Specificity of sites within eight-membered ring zeolite channels for carbonylation of methyls to acetyls, *J. Am. Chem. Soc.*, 2007, **129**, 4919–4924.

13 D. B. Rasmussen, J. M. Christensen, B. Temel, F. Studt, P. G. Moses, J. Rossmeisl, A. Riisager and A. D. Jensen, Reaction mechanism of dimethyl ether carbonylation to methyl acetate over mordenite – A combined DFT/experimental study, *Catal. Sci. Technol.*, 2017, **7**, 1141–1152.

14 M. Boronat, C. Martínez-Sánchez, D. Law and A. Corma, Enzyme-like specificity in zeolites: A unique site position in mordenite for selective carbonylation of methanol and dimethyl ether with CO, *J. Am. Chem. Soc.*, 2008, **130**, 16316–16323.

15 P. Feng, G. Zhang, X. Chen, K. Zang, X. Li and L. Xu, Specific zone within 8-membered ring channel as catalytic center for carbonylation of dimethyl ether and methanol over FER zeolite, *Appl. Catal., A*, 2018, **557**, 119–124.

16 M. Lusardi, T. T. Chen, M. Kale, J. H. Kang, M. Neurock and M. E. Davis, Carbonylation of dimethyl ether to methyl acetate over SSZ-13, *ACS Catal.*, 2019, **10**, 842–851.

17 P. Cheung, A. Bhan, G. Sunley, D. Law and E. Iglesia, Site requirements and elementary steps in dimethyl ether carbonylation catalyzed by acidic zeolites, *J. Catal.*, 2007, **245**, 110–123.

18 Y. Chu, A. Y. Lo, C. Wang and F. Deng, Origin of high selectivity of dimethyl ether carbonylation in the 8-membered ring channel of mordenite zeolite, *J. Phys. Chem. C*, 2019, **123**, 15503–15512.

19 X. B. Feng, F. Chen, Z. M. He, X. Y. Zhao and J. P. Cao, Comparison of dimethyl ether carbonylation performance over some zeolites containing 8-member ring pores, *Energy Fuels*, 2022, **36**, 14341–14348.

20 S. Liu, X. Fang, Y. Liu, H. Liu, X. Ma, W. Zhu and Z. Liu, Dimethyl ether Carbonylation over Mordenite zeolite modified by Alkyimidazolium ions, *Catal. Commun.*, 2020, **147**, 106161.

21 A. Bhan and E. Iglesia, A link between reactivity and local structure in acid catalysis on zeolites, *Acc. Chem. Res.*, 2008, **41**, 559–567.

22 Y. Chu, B. Han, A. Zheng, X. Yi and F. Deng, Pore selectivity for olefin protonation reactions confined inside mordenite zeolite: A theoretical calculation study, *J. Phys. Chem. C*, 2013, **117**, 2194–2202.

23 IZA Structure Commission, https://america.iza-structure.org/IZA-SC/ftc_table.php, (accessed December 28, 2025).

24 S. Yuan, J. Wang, Y. Li and S. Peng, Siting of B, Al, Ga or Zn and bridging hydroxyl groups in mordenite: An ab initio study, *J. Mol. Catal. A: Chem.*, 2001, **175**, 131–138.

25 Y. Li, R. Liu, Q. Guo, H. Bian, A. Lan, X. Li, P. Han and T. Dou, Efficient synthesis of high silica SSZ-13 zeolite via a steam-assisted crystallization process, *J. Porous Mater.*, 2019, **26**, 1879–1888.

26 S. Y. Park, C. H. Shin and J. W. Bae, Selective carbonylation of dimethyl ether to methyl acetate on Ferrierite, *Catal. Commun.*, 2016, **75**, 28–31.

27 N. E. Gordina, T. N. Borisova, K. S. Kiyagina, I. A. Astrakhantseva, A. A. Ilyin and R. N. Rumyantsev, Investigation of NH_3 desorption kinetics on the LTA and SOD zeolite membranes, *Membranes*, 2022, **12**, 147.

28 P. Xiao, Y. Wang, L. Wang, H. Toyoda, k. Nakamura, S. Bekhti, Y. Lu, J. Huang, H. Gies and T. Yokoi, Understanding the effect of spatially separated Cu and acid sites in zeolite catalysts on oxidation of methane, *Nat. Commun.*, 2024, **15**, 2718.

29 J. Zhu, K. Muraoka, T. Ohnishi, Y. Yanaba, M. Ogura, A. Nakayama, T. Wakihara, Z. Liu and T. Okubo, Synthesis and structural analysis of high-silica ERI zeolite with spatially-biased Al distribution as a promising NH_3-SCR catalyst, *Adv. Sci.*, 2024, **11**, 2307674.

30 K. Cai, S. Huang, Y. Li, Z. Cheng, J. Lv and X. Ma, Influence of acid strength on the reactivity of dimethyl ether carbonylation over H-MOR, *ACS Sustainable Chem. Eng.*, 2018, **7**, 2027–2034.

31 S. B. Hong, E. G. Lear, P. A. Wright, W. Zhou, P. A. Cox, C. H. Shin, J. H. Park and I. S. Nam, Synthesis, structure solution, characterization, and catalytic properties of TNU-10: A high-silica zeolite with the STI topology, *J. Am. Chem. Soc.*, 2004, **126**, 5817–5826.

32 M. Boronat, C. Martinez and A. Corma, Mechanistic differences between methanol and dimethyl ether carbonylation in side pockets and large channels of mordenite, *Phys. Chem. Chem. Phys.*, 2011, **13**, 2603–2612.

33 D. B. Rasmussen, J. M. Christensen, B. Temel, F. Studt, P. G. Moses, J. Rossmeisl, A. Riisager and A. D. Jensen, Ketene as a reaction intermediate in the carbonylation of dimethyl ether to methyl acetate over mordenite, *Angew. Chem., Int. Ed.*, 2015, **54**, 7261–7264.

34 N. Tsunoji, D. Shimono, K. Tsuchiya, M. Sadakane and T. Sano, Formation pathway of AEI zeolites as a basis for a streamlined synthesis, *Chem. Mater.*, 2019, **32**, 60–74.

35 B. W. Boal, J. E. Schmidt, M. A. Deimund, M. W. Deem, L. M. Henling, S. K. Brand, S. I. Zones and M. E. Davis, Facile synthesis and catalysis of pure-silica and heteroatom LTA, *Chem. Mater.*, 2015, **27**, 7774–7779.

36 D. Jo, T. Ryu, G. T. Park, P. S. Kim, C. H. Kim, I. S. Nam and S. B. Hong, Synthesis of high-silica LTA and UFI zeolites and NH_3–SCR performance of their copper-exchanged form, *ACS Catal.*, 2016, **6**, 2443–2447.

37 R. Shannon, R. Staley, A. Vega, R. Fischer, W. Baur and A. Auroux, Nature of the framework hydroxyl groups in steamed H-RHO and H-erionite zeolites, *J. Phys. Chem.*, 1989, **93**, 2019–2027.

38 K. Lillerud, Aluminium distribution in the zeolites offretite and erionite, *Zeolites*, 1987, **7**, 14–17.

39 F. Roessner, K. H. Steinberg, A. Rudolf and B. Staudte, Infrared spectroscopic study on the cation distribution in calcium-exchanged erionite, *Zeolites*, 1989, **9**, 371–376.

40 J. Antúnez-García, D. H. Galván, V. Petranovskii, F. N. Murrieta-Rico, R. I. Yocupicio-Gaxiola and S. Fuentes-Moyado, Theoretical study of the effect of isomorphous substitution by Al^{3+} and/or Fe^{3+} cations to tetrahedral positions in the framework of a zeolite with erionite topology, *J. Mater. Sci.*, 2019, **54**, 13190–13199.

41 J. Li, M. Gao, W. Yan and J. Yu, Regulation of the Si/Al ratios and Al distributions of zeolites and their impact on properties, *Chem. Sci.*, 2023, **14**, 1935–1959.

42 Z. Wang, Y. Jiang, O. Lafon, J. Trébosc, K. D. Kim, C. Stampfl, A. Baiker, J. P. Amoureux and J. Huang, Brønsted acid sites based on penta-coordinated aluminum species, *Nat. Commun.*, 2016, **7**, 13820.

43 P. Bräuer, P. L. Ng, O. Stiumorang, I. Hitchcock and C. D'Agostino, Effect of Al content on number and location of hydroxyl acid species in zeolites: A DRIFTS quantitative protocol without the need for molar extinction coefficients, *RSC Adv.*, 2017, **7**, 52604–52613.

44 M. Boronat and A. Corma, Factors controlling the acidity of zeolites, *Catal. Lett.*, 2015, **145**, 162–172.

45 S. Wang, S. Li, L. Zhang, Z. Qin, Y. Chen, M. Dong, J. Li, W. Fan and J. Wang, Mechanistic insights into the catalytic role of various acid sites on ZSM-5 zeolite in the carbonylation of methanol and dimethyl ether, *Catal. Sci. Technol.*, 2018, **8**, 3193–3204.

46 Y. Liu, N. Zhao, H. Xian, Q. Cheng, Y. Tan, N. Tsubaki and X. Li, Facilely synthesized H-mordenite nanosheet assembly for carbonylation of dimethyl ether, *ACS Appl. Mater. Interfaces*, 2015, **7**, 8398–8403.

47 M. Bocus, R. Goeminne, A. Lamaire, M. Cools-Ceuppens, T. Verstraelen and V. Van Speybroeck, Nuclear quantum effects on zeolite proton hopping kinetics explored with machine learning potentials and path integral molecular dynamics, *Nat. Commun.*, 2023, **14**, 1008.

48 Z. Zhao, Y. Xing, S. Li, X. Meng, F. Xiao, R. McGuire, A. Parvulescu, U. Müller and W. Zhang, Mapping Al distributions in SSZ-13 zeolites from ^{23}Na solid-state NMR spectroscopy and DFT calculations, *J. Phys. Chem. C*, 2018, **122**, 9973–9979.

49 A. Martucci, A. Alberti, G. Cruciani, P. Radaelli, P. Ciambelli and M. Rapacciulo, Location of Brønsted sites in D-ferrierite by neutron powder diffraction, *Microporous Mesoporous Mater.*, 1999, **30**, 95–101.

50 T. Lemishko, S. Valencia, F. Rey, M. Jiménez-Ruiz and G. Sastre, Inelastic neutron scattering study on the location of Brønsted acid sites in high silica LTA zeolite, *J. Phys. Chem. C*, 2016, **120**, 24904–24909.

51 C. Beauvais, X. Guerrault, F. Coudert, A. Boutin and A. Fuchs, Distribution of sodium cations in faujasite-type zeolite: Acanonical parallel tempering simulation study, *J. Phys. Chem. B*, 2004, **108**, 399–404.

52 J. Sauer, Sodium doped sodium sodalite: Magnetic coupling between F centers and hyperfine interactions with framework atoms, *Phys. Chem. Chem. Phys.*, 1999, **1**, 4505–4514.

53 H. Trill, H. Eckert and V. Srdanov, Topotactic transformations of sodalite cages: Synthesis and NMR study of mixed salt-free and salt-bearing sodalites, *J. Am. Chem. Soc.*, 2002, **124**, 8361–8370.

54 R. Fletcher, S. Ling and B. Slater, Violation of Löwenstein's rule in zeolites, *Chem. Sci.*, 2017, **8**, 7483–7491.

55 G. Engelhardt and D. Michel, *High-resolution solid-state NMR of silicates and zeolites*, Wiley, New York, 1987.

56 W. Chen, K. A. Tarach, K. Góra-Marek and A. Zheng, Confinement driving mechanism of surface methoxy species formation in mordenite zeolite: An interplay of different molecular factors, *Appl. Catal., B*, 2024, **357**, 124306.

57 Y. Jiang, M. Hunger and W. Wang, On the reactivity of surface methoxy species in acidic zeolites, *J. Am. Chem. Soc.*, 2006, **128**, 11679–11692.

58 W. Chen, Z. Liu, X. Yi and A. Zheng, Confinement-driven dimethyl ether carbonylation in mordenite zeolite as an ultramicroscopic reactor, *Acc. Chem. Res.*, 2024, **57**, 2804–2815.

59 Z. Liu, X. Yi, G. Wang, X. Tang, G. Li, L. Huang and A. Zheng, Roles of 8-ring and 12-ring channels in mordenite for carbonylation reaction: From the perspective of molecular adsorption and diffusion, *J. Catal.*, 2019, **369**, 335–344.

60 W. Wang, W. Qian, H. Ma, W. Ying and H. Zhang, A theoretical study on the feed ratio of dimethyl ether carbonylation on H-MOR zeolites, *Mol. Phys.*, 2021, **119**, e1896044.

61 A. M. Ukpong, First principles study of van der Waals heterobilayers, *Comput. Condens. Matter*, 2015, **2**, 1–10.

62 A. Kiejna, T. Pabisiak and S. Gao, The energetics and structure of rutile TiO_2 (110), *J. Phys. Condens. Matter*, 2006, **18**, 4207.

63 X. Ma, Y. Wu, Y. Lu and Y. Zhu, Correlation effects on lattice relaxation and electronic structure of ZnO within the GGA+U formalism, *J. Phys. Chem. C*, 2013, **117**, 26029–26039.

64 J. Sun, R. C. Remsing, Y. Zhang, Z. Sun, A. Ruzsinszky, H. Peng, Z. Yang, A. Paul, U. Waghmare and X. Wu, Accurate first-principles structures and energies of diversely bonded systems from an efficient density functional, *Nat. Chem.*, 2016, **8**, 831–836.

65 P. Maragakis, S. A. Andreev, Y. Brumer, D. R. Reichman and E. Kaxiras, Adaptive nudged elastic band approach for transition state calculation, *J. Chem. Phys.*, 2002, **117**, 4651–4658.

66 J. A. Garrido Torres, P. C. Jennings, M. H. Hansen, J. R. Boes and T. Bligaard, Low-scaling algorithm for nudged elastic band calculations using a surrogate machine learning model, *Phys. Rev. Lett.*, 2019, **122**, 156001.

67 H. Aljama and F. Abild-Pedersen, Accessing the C–C transition state energy on transition metals, *Phys. Chem. Chem. Phys.*, 2019, **21**, 25328–25333.

68 R. Kronberg, H. Lappalainen and K. Laasonen, Revisiting the Volmer–Heyrovský mechanism of hydrogen evolution on a nitrogen doped carbon nanotube: Constrained molecular dynamics versus the nudged elastic band method, *Phys. Chem. Chem. Phys.*, 2020, **22**, 10536–10549.

69 K. Sun, Y. Zhao, H. Y. Su and W. X. Li, Force reversed method for locating transition states, *Theor. Chem. Acc.*, 2012, **131**, 1–10.